Research article

Enhanced light management and optimization of perovskite solar cells incorporating wavelength dependent reflectance modeling

Shahriyar Safat Dipta [*], Ashraf Uddin [*], Gavin Conibeer

School of Photovoltaic and Renewable Energy Engineering, University of New South Wales, Sydney, NSW 2052, Australia

HIGHLIGHTS

- Simulation of Perovskite solar cells with MgF2 ARC to optimize light management.
- Improving the simulation of SCAPS-1D based solar cell studies by incorporating reflectance modelling, which is ignored in all previous studies.
- Detailed analysis of loss of photons from non-radiative recombination in PSC studies.
- Optimization of the device to improve the efficiency to greater than 20%.

ARTICLE INFO

ABSTRACT

Perovskite Solar Cells (PSCs) are the most promising candidates for low-cost and high-efficiency devices in the future photovoltaic market. PSCs are also used as the top cell in tandem devices with silicon bottom cells. However, research in PSCs is still at an early stage while racing towards a promising future. Along with experimental research, numerous simulation studies are conducted with PSCs aiming to analyze new materials and optimize their performance. Here, a wavelength-dependent model is implemented to account for the reflected part of irradiance from the cells, which is ignored in most SCAPS-1D based PSC simulated models. This model optimizes the MgF_2 anti-reflective coating in SCAPS-1D simulation to allow maximum photons to pass inside the device. A simple structured PSC (MgF_2/Glass/ITO/ZnO/$CH_3NH_3PbI_3$/Spiro-OMeTAD/Au) is simulated and optimized optically as well as electrically with this model's modified spectrum. The device was optimized for layer thickness, defects, and doping. Moreover, the effects of temperature and device resistances are discussed. The optimized device yields 21.62% power conversion efficiency, which can be further improved to reach over 25% through better processing schemes. Finally, the optimized device was compared with other devices having different ETL/absorber/HTL combinations and the pathway to achieving higher efficiencies was discussed. This article aims at improving the credibility of simulated devices by incorporating top surface reflection with electrical optimization.

1. Introduction

Research in perovskite solar cells (PSCs) escalated in the last decade and is expected to follow the same pattern for the next few years. PSCs have convincingly shown potential to be placed side by side with silicon solar cells in the market and space applications [1]. Perovskites have multiple properties well suited for photovoltaic (PV) applications, such as bandgap tunability, high absorption coefficient, high carrier mobilities, facile fabrication routes, and low material cost [2, 3, 4, 5]. Such convenient properties attracted numerous researchers to study and contribute to this field. However, research in PSCs is still not mature, and there are

enough opportunities for improvement in this field. Though the first research on perovskites goes way back to 1839, the first published article on perovskites for PV application was in 2009 [6, 7]. The efficiency of the first PSC was 3.1% which gradually improved to more than 25% as of 2022 [8, 9].

There was only experimental research in the early stage of this class of PV technology. However, many simulation works of PSCs have been published in recent years [10, 11, 12]. In most of these articles, the thickness of different layers, doping profile, defect concentration in materials and interfaces, and device resistances (series and shunt) are varied to optimize the device [13, 14]. All the Solar Cell Capacitance

---

Simulator (SCAPS-1D) simulation studies assume zero reflectance from the top surface of the devices. Zero reflectance is also the default setting of the SCAPS-1D, which has been used in almost all the simulated articles on PSCs using this simulator. Moreover, the refractive indices of the materials are also not taken as a parameter that might suggest that the simulator internally measures the reflectance. For this reason, there has been a particular discrepancy in performance parameters in the results of simulation using SCAPS-1D and experimental data. Avoidance of reflectance often results in an overestimation of the performance of the cells. Dong et al. experimentally optimized the device using silica glass as the anti-reflective coating (ARC) [15]. Some part of the spectrum was lost due to reflection even in the optimized device. Apart from this, there has been no detailed study on optimizing light management in PSCs.

This study modified the AM1.5G solar spectrum by introducing a wavelength-dependent reflectance model to feed into the simulator. MgF$_2$, having a refractive index of approximately 1.38 for all wavelengths of interest (250 nm–850 nm), works as an excellent ARC for PSCs. Moreover, the thickness of the MgF$_2$ layer was adjusted to allow the least amount of reflection loss. Fresnel equations were used to analytically calculate the reflectance from the top MgF$_2$ surface, MgF$_2$/Glass interface, glass/ITO interface, and ITO/ZnO interface. Moreover, wavelength-dependent phase difference was calculated analytically to find the extent of constructive or destructive interference at all wavelengths from 250 to 850 nm. Eqs. (1)a, (1)b and (1)c have been used to calculate the overall reflectance.

$$R = \left| \frac{n_1(\lambda) - n_2(\lambda)}{n_1(\lambda) + n_2(\lambda)} \right|^2 \tag{1a}$$

$$T = 1 - R \tag{1b}$$

$$\Delta\Theta = \frac{4\pi d}{\lambda} \tag{1c}$$

Here, $n_1(\lambda)$ and $n_2(\lambda)$ are the refractive index of the two media that forms the interface, R is the reflectance, T is the transmittance, $\Delta\Theta$ is the phase difference, d is the thickness of the layer, and λ is the wavelength of light. Destructive interference will occur if the phase difference is an odd multiple of π [16]. The phase difference is dependent on the thickness of the ARC. Therefore, the thickness of the ARC was varied to find the optimized spectrum for the device model.

The number of simulation papers on PSCs is rapidly increasing. Since the modelling and simulation of PSC devices are still in the early stages, there is a lot to improve. This study contributes to the literature showing the right path to simulate the devices accommodating the reflected part in SCAPS-1D. This work analyzed light management and optimization of ARC for the first time in PSC simulation studies with SCAPS-1D. Though optical simulation has been done in many studies, none of the SCAPS-1D studies currently incorporate optical modelling to account for top surface reflectance. The result obtained by following this method matches better with experimental devices. Optimization from simulation can also be applied to find the thickness of the top MgF$_2$ layer that accounts for minimum overall reflectance. This study shows the optimization path for the typical PSC having MgF$_2$/Glass/ITO/ZnO/MAPbI$_3$/Spiro-OMeTAD/ Au structure. This work also explains non-radiative recombination from the device's band diagram and carrier generation-recombination profile interfaces. Moreover, this study also optimizes the devices with different electron transport layers (ETLs), hole transport layers (HTLs) and absorber layers to compare and find the best combination.

2. Device structure and simulation methods

2.1. Control device structure

A perovskite solar cell has three main layers, the electron transport layer, the absorber perovskite layer, and the hole transport layer. In this work, the control device uses Al-doped ZnO as the ETL, MAPbI$_3$ as the absorber, and Spiro-OMeTAD as the HTL. Apart from this, Au acts as the back electrode, ITO as the front electrode, and MgF$_2$ as the ARC. The schematic of the modelled device is shown in Figure 1.

2.2. Defining material parameters

The materials used in the control device are shown in Figure 1. Subsequently, several other absorbers, ETLs, and HTLs are used for the simulations. For absorbers, other materials used are MAPbBr$_3$, FASnI$_3$, and CsFAPb(Br$_x$I$_{1-x}$)$_3$. Different ETL such as TiO$_2$ and SnO$_2$ are used. Finally, HTLs used in the simulations include NiO$_X$, P3HT, and Cu$_2$O. The parameters for all these materials used in the simulation are shown in Table 1.

2.3. Simulation methods

Simulation in this work comprises of two parts. In the first part, the reflectance and transmittance of the device are calculated analytically to optimize for the least top surface reflection. In this part, analytical calculations were performed for finding transmittance as a function of the thickness of the ARC using Eqs. 1(a)–1(c), and the corresponding modified spectrum energy was generated [16]. For each interface, wavelength-dependent transmitted and reflected portions are calculated from Eqs. (1a) and (1b). Next, the phase travelled by the transmitted photons in the next layer is calculated using Eq. (1c). The same calculations are performed for the first three interfaces, after which the reflectance is negligible due to absorption in the active layer. Finally, overall reflectance is calculated using destructive interference theory [16] for each wavelength to obtain the modified spectrum. This modified spectrum is used for simulation instead of the standard AM1.5G spectrum.

The second portion of the simulation is performed in Solar Cell Capacitance Simulator (SCAPS-1D) software which was developed by the University of Gent, Belgium. SCAPS has several built-in spectrums for AM1.5G light. However, SCAPS does not calculate wavelength-dependent reflectance. The modified spectrum generated in the previous part was used as the input light spectrum for the entire optical and electrical simulation by SCAPS. For simulating a device, SCAPS solves Poisson's Eq. (2a), the continuity Eqs. 3(a) and (b) for electrons and holes, and the drift-diffusion Eqs. 4(a) and (b) for electrons and holes as shown below.
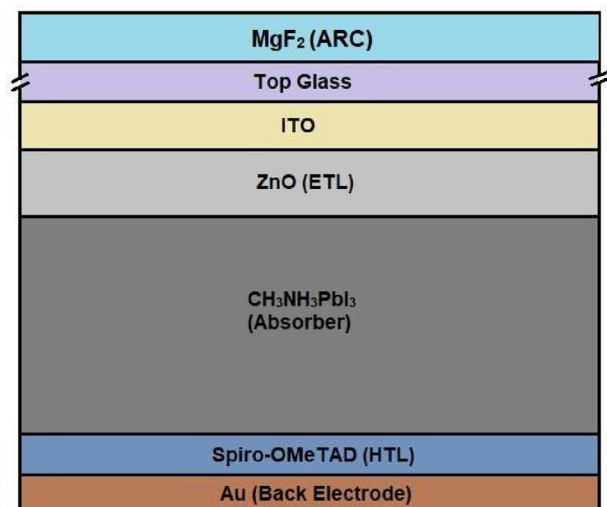
Poisson's equation:

Figure 1. Schematic representation (not to scale) of the side view of the modelled PSC with initially used materials for the control device.

Table 1. Initial material parameters used in this work before optimization.

Properties	ITO [17, 18]	Al–ZnO [19]	MAPbI$_3$ [20,21]	Spiro-OMeTAD [22, 23]	MAPbBr$_3$ [24]	FASnI$_3$ [24]	CsFAPb (Br$_x$I$_{1-x}$)$_3$ [25]	TiO$_2$ [26]	SnO$_2$ [22]	NiO$_x$ [10]	P3HT [12]	Cu$_2$O [27]
Thickness (nm)	100	60	320	100	600	350	300	30	30	100	70	100
Bandgap (eV)	3.5	3.2	1.55	2.91	2.3	1.41	1.59	3.2	3.5	3.5	1.85	2.17
Affinity (eV)	4	4	3.9	2.2	3.9	3.52	4.09	4	4	2.2	3.1	3
Permittivity	9	8.5	6.5	3	6.5	8.2	6.6	9	9	9	3.4	7.11
N$_C$ (cm^{-3})	2E18	2.2E18	2.2E18	2E19	2.2E18	1E18	2E19	2.1E18	2E18	2.2E18	1E22	2.2E18
N$_V$ (cm^{-3})	1E19	1.8E19	1.8E19	2E18	1.8E19	1E18	2E18	1.8E19	1.8E19	1.8E19	1E22	1.1E19
Electron Thermal Velocity (cm/s)	1E7	1E7	1E7	1E7	1E7	1E7	1E7	1E7	1E7	1E7	1E7	1E7
Hole Thermal Velocity (cm/s)	1E7	1E7	1E7	1E7	1E7	1E7	1E7	1E7	1E7	1E7	1E7	1E7
Electron Mobility (cm^2/V-s)	20	166	20	.01	20	22	8.16	20	20	4.7	1E-4	200
Hole Mobility (cm^2/V-s)	10	30	10	.01	20	22	2	10	10	4.7	1E-4	80
N$_D$ (cm^{-3})	2E19	1E16	0	0	0	0	0	9E16	1E16	0	0	0
N$_A$ (cm^{-3})	0	0	0	1E16	0	0	0	0	0	1E16	1E18	1E16
Defect Type	Neutral	Neutral	Neutral	Neutral	Neutral	Neutral	Neutral	Neutral	Neutral	Neutral	Neutral	Neutral
Capture cross-section (Electron and hole)	1E-15	1E-15	1E-15	1E-15	1E-15	1E-15	1E-15	1E-14	1E-14	1E-15	1E-15	1E-15
Energy Distribution	Single	Single	Single	Single	Single	Single	Single	Single	Single	Single	Single	Single
Energy level above Ev (eV)	0.6	0.6	0.2	0.6	0.2	0.3	0.3	0.6	0.6	0.4	0.4	0.6
Nt (cm^{-3})	1E15	1E15	2E15	1E14	2E15	2E15	1E15	1E15	1E14	1E14	1E14	1E15

$$\frac{d^2}{dx^2}\psi(x) = \frac{e}{\varepsilon_0\varepsilon_r}\left(p(x) - n(x) + N_D - N_A + \rho_p - \rho_n\right) \tag{2a}$$

Here Ψ(x), e, ε_r, ε_0, p, n, N_D, N_A, ρ_p, and ρ_n denote electrostatic potential, electrical charge, relative permittivity, vacuum permittivity, hole concentration, electron concentration, donor concentration, acceptor concentration, hole distribution, and electrons distribution, respectively.

Carrier continuity equations:

$$\frac{dJ_n}{dx} = G - R \tag{3a}$$

$$\frac{dJ_p}{dx} = G - R \tag{3b}$$

Here J_n, J_p, R, and G are electron and hole current densities, recombination rate, and generation rate, respectively.

Drift-diffusion equations:

$$J_n = D_n\frac{dn}{dx} + \frac{d\varphi}{dx} \tag{4a}$$

$$J_p = D_p\frac{dp}{dx} + \frac{d\varphi}{dx} \tag{4b}$$

Here D_n and D_p represent the electron and hole mobilities, respectively.

From the results of SCAPS, the current density (J) vs voltage (V) curve, the Quantum efficiency (QE) curve, the band diagrams, and the electron-hole pair generation-recombination curves were analyzed to optimize the device in terms of thickness of the devices, the doping in each layer, and defect density within practical limits.

3. Optical simulation and light management

3.1. Standard AM1.5G spectrum

AM1.5G spectrum is the most used solar spectrum in simulations. Though SCAPS has several files for the AM1.5G spectrum, some discrepancies exist with the original spectrum. For this reason, the spectrum for this simulation was taken from the National Renewable Energy Laboratory website [28, 29]. The global tilt version, which consists of both direct and diffused light, was the spectrum used for this study. The energy of this spectrum as calculated was 1000 W/m^2, which is reasonably

close to the standard value of the AM1.5G spectrum. This spectrum having irradiance of 1000 W/m^2 was used to analyze transmittance and reflectance from the device.

3.2. Reflection of light from the device

Without employing an anti-reflective layer, a considerable part of incident photons will reflect from the top Glass and ITO surfaces. The amount of reflection will depend on the wavelength of light and the refractive index of the cell's top layer (ITO). Figure 2 shows the amount of reflectance without using an anti-reflective coating determined by destructive interference theory [30]. From the analytical calculation of transmitted power, it is found that 13% of energy from sunlight is reflected from the top surface, which does not contribute to the power output.

3.3. Optimization of reflection by using anti-reflective coating

The anti-reflective coating helps to reduce reflection from a solar cell. The anti-reflective action depends on the wavelength of light, the thickness of the anti-reflective coating (ARC), and the materials'
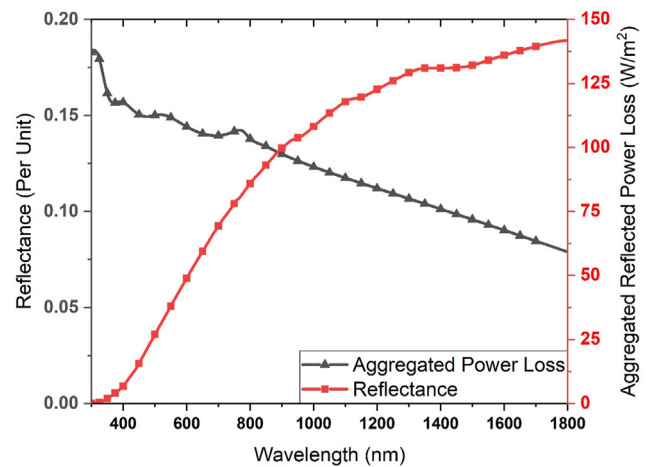
Figure 2. Theoretical wavelength-dependent reflection from the modelled PSC's top surface without an anti-reflective layer along with the aggregated amount of power lost through top reflection.

refractive indices. ARC reduces the reflectance of light from the surface through destructive interference for a particular wavelength, given that the thickness of the layer is an odd multiple of $\lambda/4$. However, the refractive index of the ARC should ideally be the geometric mean of the medium light comes from and the layer just beneath the ARC. Otherwise, partial destructive interference will occur for that wavelength. Since light comes from air in the case of solar cells, the ideal refractive index in the modelled structure is the square root of the ITO layer. Therefore, for destructive interference, the refractive index and the thickness of the ARC are given below in Eqs. (5a) and (5b).

$$n_{arc} = \sqrt{n_1} \tag{5a}$$

$$t_{arc} = \lambda/4 \tag{5b}$$

Here, n_{arc} and n_1 are the refractive indices of the ARC and the next layer (ETL), t_{arc} is the thickness of the ARC, and λ is the wavelength of light. In perovskite solar cells, SiO_2 (silica glass) with a refractive index of approximately 1.5 and thickness of 1.1–1.2 mm is used as the substrate. A spin-coated or thermally evaporated thin film of MgF_2 nanostructures with a refractive index of 1.38 on the opposite side of ITO works as the ARC for PSCs in real devices [31]. Though SiO_2 is optically more suitable than MgF_2 as the ARC, the thickness does not allow it to use as the ARC. The refractive index of MgF_2 (1.38) is also very near the ideal value of ARC within the wavelength of interest (300 nm–800 nm) as depicted by Figure S1. Figure S1 depicts the refractive indices of ITO, SiO_2, MgF_2, and the ideal refractive index at different wavelengths.

Moreover, the thickness of the ARC will dictate the amount of light lost through reflection. An optimum thickness of the ARC is necessary to trap the maximum possible portion of incident sunlight. Therefore, calculations were performed for reflectance as a function of the thickness of the ARC, and the results are shown in Figure 3. Results in Figure 3 show the reflectance is reduced to zero at some wavelengths for every thickness. At these wavelengths, the conditions of both Eqs. (5a) and (5b) were met, allowing total destructive interference. Too thin ARC causes higher reflectance throughout the spectrum, and higher thickness values account for higher reflectance in short-wavelength parts. From Figure 3 80 nm and 100 nm thick ARC give the lowest reflection, and thus they are more suited for optimum light trapping of the cells.

Next, the power intensity of light going through the cells was calculated by deducting the reflected part from the initial spectrum. Power intensity was calculated using Eq. (6), where $I(\lambda)$ is the irradiance at a particular wavelength and $R(\lambda)$ is the reflectance at that wavelength for a particular ARC thickness. AM1.5G spectrum that we used has a power of 1000 W/m². Figure 4 shows the effective irradiance passing inside the cells for different ARC thicknesses. From calculated values, the optimum thickness of the ARC is 100 nm, for which only 16.92 W/m² of power was reflected, less than 2% of total incident power. The amount of power intensity in the modified spectrum was 983.08 W/m².

$$Power\ Intensity = \int I(\lambda)(1 - R(\lambda))d\lambda \tag{6}$$

3.4. Modified AM1.5G spectrum

For SCAPS, light transmittance is set at 100% by default, and the wavelength-dependent transmittance feature is unavailable. Therefore, the original AM1.5G spectrum was modified by deducting the reflected portion of light. It is noteworthy that the modification was done in the spectrum only for wavelengths less than 800 nm since perovskites used throughout this work do not absorb photons of wavelengths longer than 800 nm. This modified spectrum was then fed to SCAPS for simulation, which assumes that all of it is transmitted. Figure S2 shows the original AM1.5G spectrum and the modified spectrum for ARC of 10 nm, 100 nm and 150 nm thicknesses.

The reflected portion of the light is observed in both the power of the modified spectrum and spectral density. The modified version originating from the original AM1.5G spectrum for 100 nm thick ARC was used for the subsequent simulations of this work.

4. Results and discussion

SCAPS simulates the generation and recombination of light and transport of the charge carriers. Therefore, it provides the J-V curves and Quantum Efficiency (QE) curves for each simulation. Moreover, generation-recombination profiles and device band diagrams can also be generated. In this chapter, the initially designed cell is optimized for the
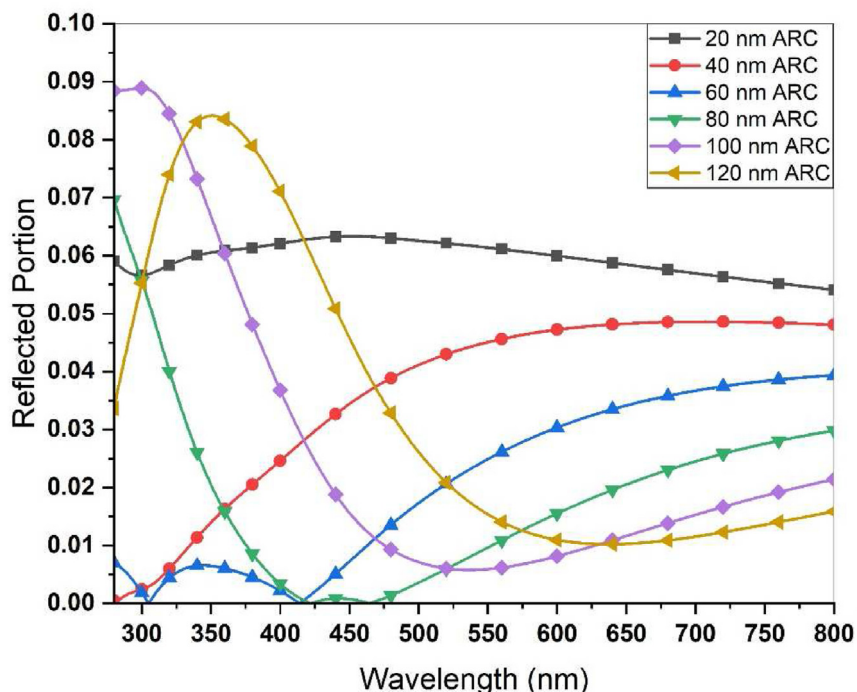
Figure 3. Portion of reflected light based on MgF_2 ARC thickness from 20 nm to 120 nm. The optimum thickness of the ARC lies between 80 nm and 100 nm.
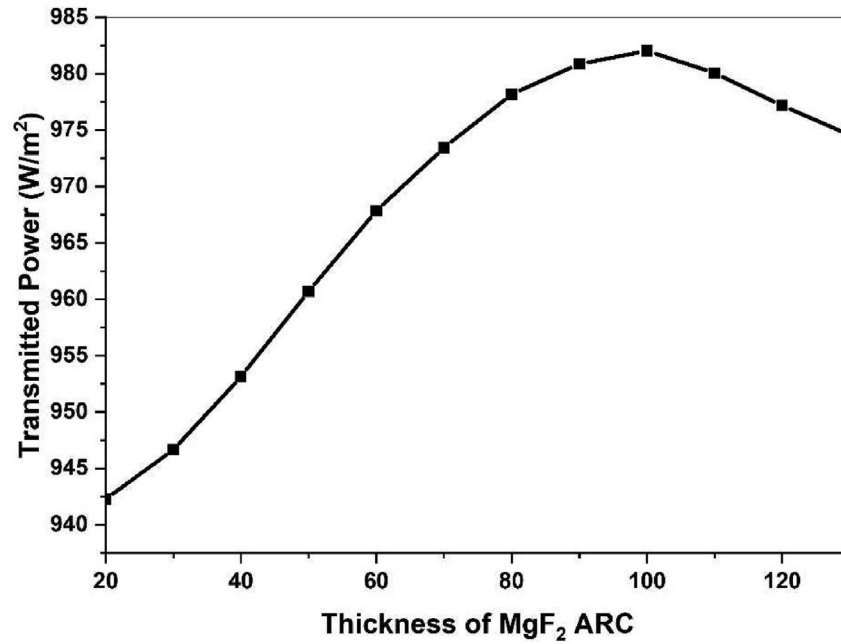
Figure 4. Effective irradiance per unit area as a function of the thickness of ARC after the reflected part is filtered out.

thicknesses of different layers, doping concentration of different layers, defect density, and defect position. The effect of temperature on the performance of the device, as well as the effect of device resistances (Series resistance and shunt resistance) are discussed at the end of this section.

4.1. Control device performance and validation

The control device had the same structure and device parameters as in the experimental paper by Khalid et al. [32, 33]. In the performance parameters, some differences in the open-circuit voltage V_{OC} and short circuit current J_{SC} are observed in the resulting J-V curves. It is predicted that the experimental device produced less J_{SC} since the ARC was not optimized, leaving a lower portion of available light for the cells to absorb. Moreover, a higher V_{OC} in the experimental device is attributed to the fabrication schemes, which produced fewer defect states than the typical values in simulation. Figure 5(a), and (b) depicts the J-V curve

and QE curve of the control device. A discrepancy in the fill factor is seen in the simulation study from the experiment. The experimental fill factor is lower than the simulated one. Though the series and shunt resistances are kept the same, the authors believe this difference is due to lower ETL/absorber defect density in the experimental study than the value used in simulation [33]. Thermal deposition of the back contact rather than manual deposition can lead to a better fill factor, which would be quite similar to the simulated one. The efficiency of the simulated control device is 8.13%, and that of the experimental work of Khalid et al. [33] is 8.25%. The unoptimized device shows much lower efficiency compared to recent PSCs. The lower efficiency is primarily due to high ETL/absorber interfacial defects, poor parasitic resistances, higher non-radiative recombination, and ion migration at the interfaces. Over the years, these have been improved in real devices by improved processing schemes, suitable additives, and optimizing solution and deposition parameters.

The QE curve shows that the efficiency is not high enough in the regions between 400 and 700 nm which is the central absorbance region
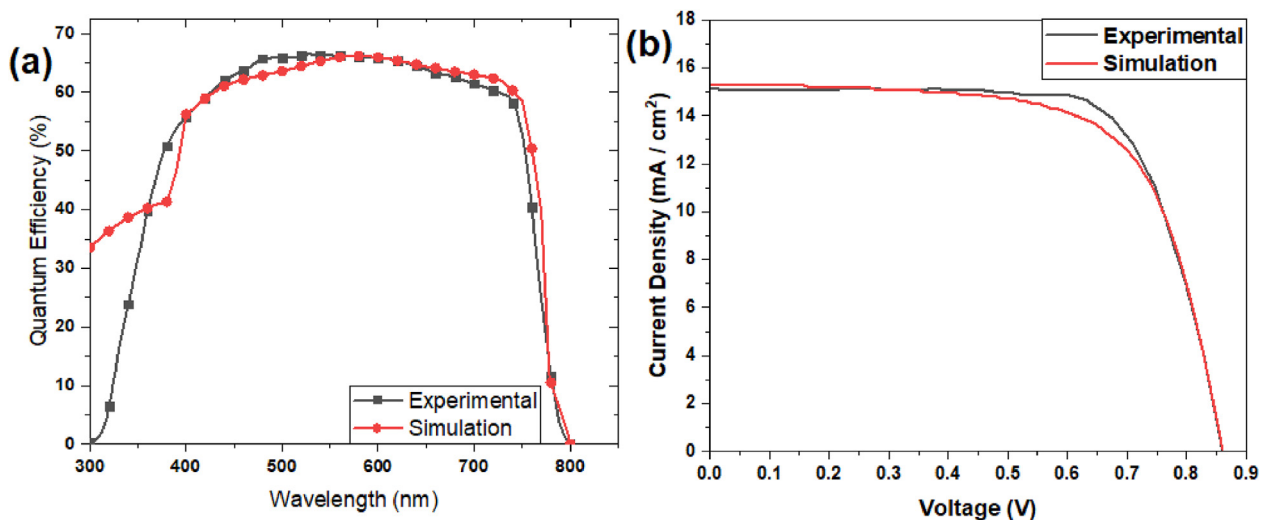

Figure 5. (a) J-V and (b) Quantum Efficiency (Internal) curves of the control device from SCAPS simulation. The experimental J-V and QE curves are plotted along with the simulated results.

for perovskite solar cells. Moreover, the QE is higher in the simulated device in the range of 300–400 nm. The higher QE in this part comes from the parasitic absorption in other layers, which is one of the limitations of SCAPS. The generation-recombination profile was generated in SCAPS to investigate the losses in this region. Figure 6(a) and (b) shows the band diagram and generation-recombination profiles of the control device.

The generation-recombination profile depicts that recombination is highest at the HTL site owing to the low carrier mobility of Spiro-OMeTAD. Spiro-OMeTAD is notorious for low carrier mobilities, encouraging researchers to look for more suitable HTLs [34]. High doping of the HTL can result in better conductivity, which yields higher efficiency. However, too high doping has a detrimental effect on the stability of the cells [35]. Moreover, there is a great deal of recombination at the ETL and an abrupt recombination change at the ETL/Absorber interface. This change was resulted from high defect density at the interface of ETL and perovskite. Reducing the non-radiative recombination is crucial for obtaining high-efficiency PSCs. Optimization was done in the subsequent simulations of this article to improve the device to yield higher efficiency.

4.2. Effect of defect density at ETL/absorber and absorber/HTL interface

The high defect density at the ETL/Absorber interface has resulted from the formation of pinholes and the non-uniform formation of the perovskite layer [36, 37]. Moreover, the accumulation of charges at the interfaces with the perovskite layer causes higher defect sites and hysteresis in the device [38]. In recent years, different groups have successfully reduced these defects by adding a spacer layer, passivating the interfaces, and improving fabrication schemes [39]. All these novelties aim at improving the interface by passivating the defects and grain boundaries. The device was simulated with varying the defect density at the ETL/absorber interface. Figure 7 depicts the performance parameters of the devices at different defect densities. Efficiency remains constant for defect densities less than 10^{12} cm^{-3}. Ideally, the efficiency can be as high as 13.84% by passivating the ETL/perovskite interface defects.

For optimization, the defect density at the ETL/absorber interface was changed to 10^{13} cm^{-3} which yields an efficiency of 11.26%, improving from the initial 8.13%. It is mentionable that the QE curve did not have any effect due to a change in interface density. It shows that interface defects do not hinder absorption but work as a barrier to the transport of charge carriers. A similar study on the defect density of the absorber/HTL interface did not affect the performance parameters over the range of 10^{11}–10^{18} cm^{-3}. However, it is desired to passivate the perovskite/HTL defects as well for better device stability.

4.3. Optimizing absorber layer thickness

The thickness of the absorber layer is a crucial parameter for the design of any high-efficiency solar cell. Too thin devices cannot absorb all the incident photons, whereas too thick devices account for increased recombination within the absorber layer [40]. Therefore, an optimal thickness is crucial for high-performance cells. The thickness of the absorber perovskite layer was changed from 100 nm to 2000 nm, and the optimum thickness was found at 800 nm. The efficiency at 800 nm thick absorber is 11.67%. Figure 8 shows the performance parameters at different thicknesses. The V_{OC} value increases with the increase of thickness, whereas the J_{SC} value increases up to 500 nm and then decreases. The increase in V_{OC} and J_{SC} is due to the absorption of more photons. Interestingly, the fill factor decreases up to 400 nm thick devices and increases with a further increase in thickness. Initially, the fill factor decreases due to the additional series resistance coming from a thick absorber. However, it goes up slightly after 500 nm due to increased V_{OC} with increasing thickness. SCAPS does not account for the reflectance from the back electrode, whereas in real devices, a portion of unabsorbed photons is reflected back. Therefore, the optimum thickness of real devices should be nearly half of the simulated optimized thickness. The optimized thickness of the simulated device is 800 nm. This corresponds to a 400 nm thick photoactive layer in real devices, which is well within the range of thickness used for lab-based cells.

For further investigation of the absorption of photons, the QE curves of the device at 100 nm, 800 nm and 1800 nm thickness are generated. Figure 9 shows that the quantum efficiency is low for thin devices at longer wavelengths, and for thick devices, it is low at shorter wavelengths of light. The absorption coefficients of perovskites are higher at shorter wavelengths, allowing much higher quantum efficiency at these wavelengths in thinner devices. However, the absorbance increases at longer wavelengths with increasing thickness, whereas the increase is minimal at shorter wavelengths. In thicker devices, recombination also plays a part and reduces the quantum efficiency at all wavelengths. Therefore, the quantum efficiency is lower for thicker devices at shorter wavelengths, and the opposite trend is followed for longer wavelengths, as depicted in Figure 9. For 400 nm wide devices, which is the optimum thickness for this structure, the overall QE is better than both 50 nm and 900 nm thick devices.
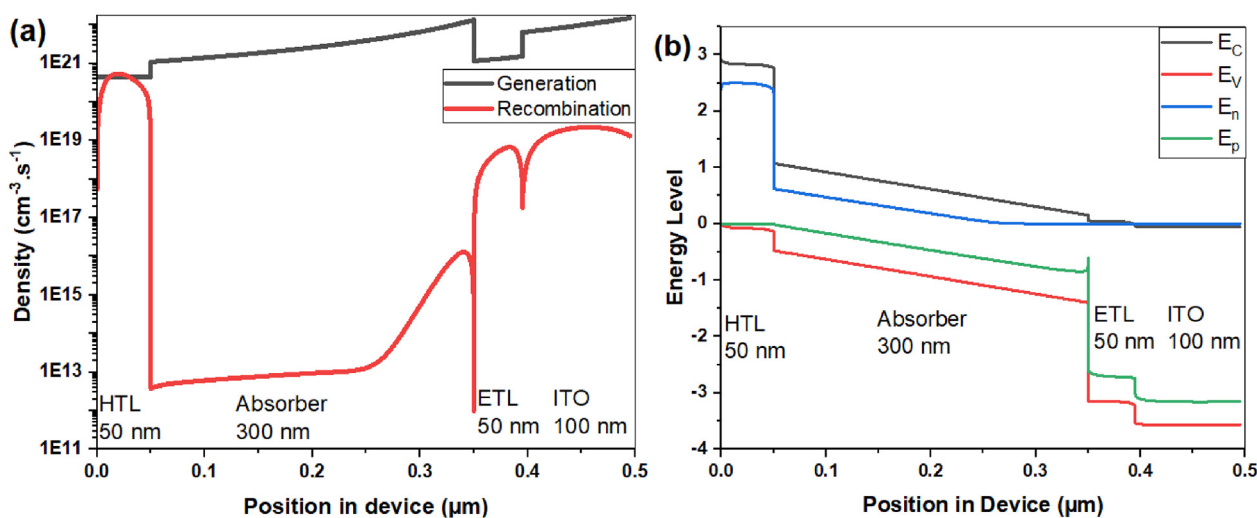

Figure 6. (a) Generation-Recombination profile, (b) Band diagram of the control device having ITO/ZnO/CH$_3$NH$_3$PbI$_3$/Spiro-OMeTAD structure (from right to left in the plots) from SCAPS simulation.
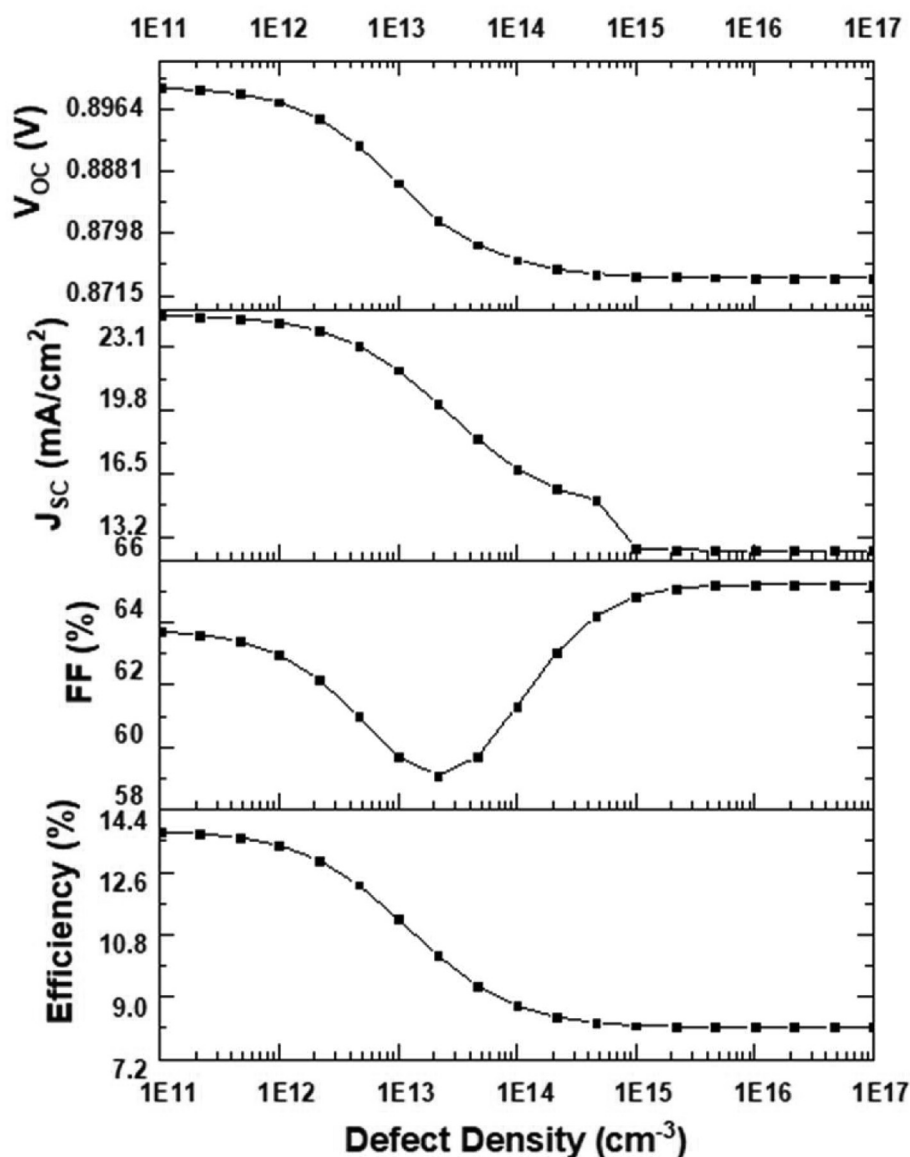
Figure 7. Device performance parameters V_{OC}, J_{SC}, FF and Efficiency as a function of ETL/absorber interface defect densities.

4.4. Optimizing thickness of other layers

The thickness of the ITO, ETL, and HTL layers has minimal effects on the device's performance since there is no main absorbing layer. However, the parasitic absorption and recombination in these layers account for a change in the efficiency of the device. Keeping the absorber at 800 nm thickness, the thickness of ETL, HTL and ITO were changed within practical limits. The results show that thin ITO and HTL provide better efficiency. For both cases, V_{OC} and FF decrease with thickness and J_{SC} increases. However, very thin HTL does not give a uniform coating, whereas thinner ITO does not conduct laterally. The thickness of ITO and HTL are kept at 100 nm and 50 nm for subsequent simulations. Moreover, the results from varying the thickness of the ETL were interesting. As depicted in Figure S3, both V_{OC} and J_{SC} increase while FF decreases with layer thickness. Overall efficiency decreases for thick ETL due to a severe decrease in the fill factor. For practical considerations involving series resistance and parasitic absorption, the thickness of the ETL was selected as 100 nm for the optimized device, which yields 11.75% efficiency.

The QE curves were observed for three different thicknesses to investigate the parasitic absorption with increasing ETL thickness. As shown in Figure S4, light absorption (overall) is greater in the short-wavelength spectrum for lower thickness, while it is more inadequate for longer wavelengths and vice versa. This trend is due to the absorption coefficient of Al-doped ZnO and the recombination in this layer. The absorption coefficient shows that Al-doped ZnO has a high value at shorter wavelengths. For thicker layers, recombination increases, and eventually, it reduces the quantum efficiency. However, the ZnO ETL thickness in real devices is typically less than 100 nm. Thicker devices have difficulty maintaining uniformity, and they create more defects in the boundaries. Moreover, marginal quantum efficiency beyond the absorption window of $MAPbI_3$ is due to the shallow defects and doping states [41]. The increase of V_{OC} is minimal and is related logarithmically to light absorption. The decrease in FF is due to the rise of series resistance which causes the J-V curve to have a smaller slope near the open circuit condition.

4.5. Effect of doping density of different layers

Doping density directly affects carrier mobility and recombination [42, 43]. Highly doped ETL with n-type charge carriers and HTL with p-type charge carriers limit non-radiative recombination losses and cause swift transport of charge carriers. This work changed the doping of ETL
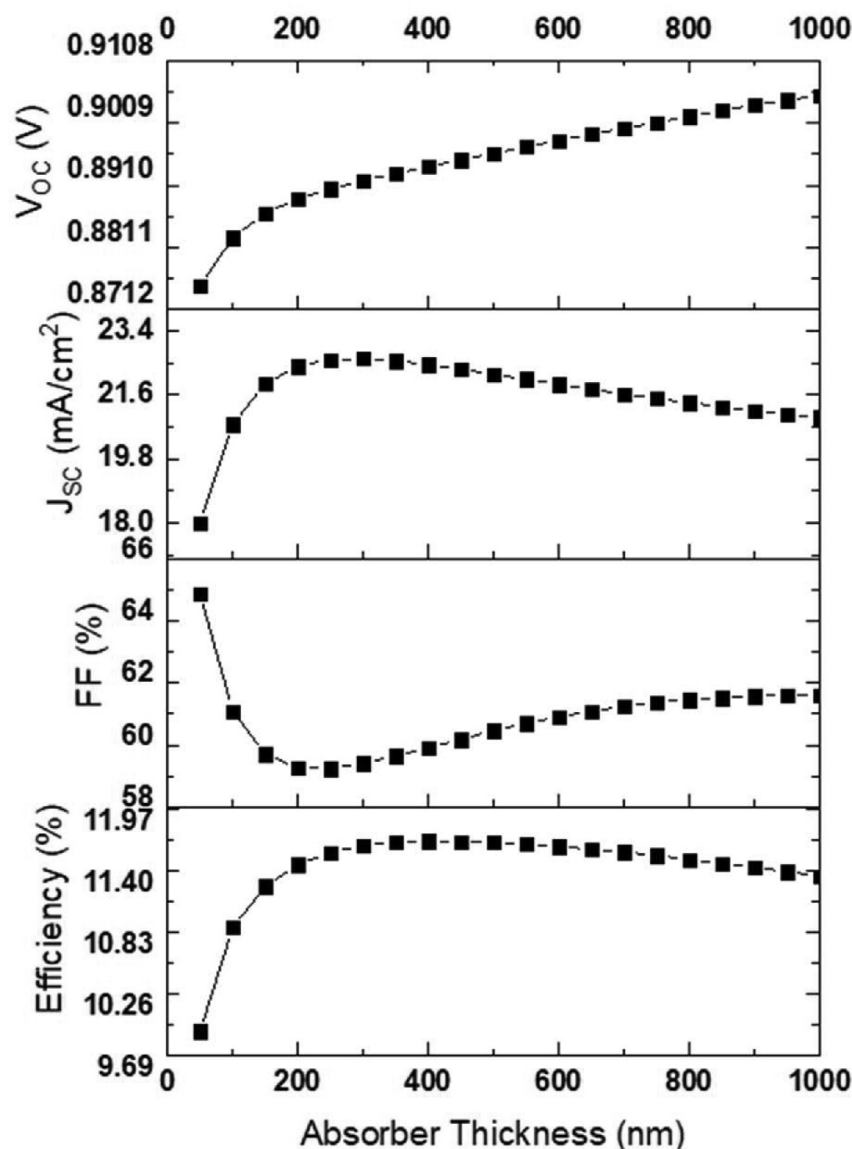
Figure 8. Performance of the modelled device as a function of the absorber layer thickness from 50 nm to 1000 nm.

and HTL within 10^{13}–10^{21} cm^{-3} to optimize the model. Figure 10(a) and (b) shows the performance parameters with different doping densities of ETL and HTL. For HTL, the efficiency gets saturated at 10^{20} cm^{-3} doping which is expected. Interestingly for ETL, the efficiency is maximum at a doping density of 10^{20} cm^{-3}, which decreases with further doping. Upon investigating the band diagram, it was seen that too high doping elevated the conduction band edge of ZnO (ETL) above the perovskite conduction band. Elevated ZnO conduction band edge causes higher recombination and barrier for electrons to pass towards the ZnO layer from the perovskite layer. Though the unoptimized device had a very high V$_{OC}$ loss, a large portion of the loss was recovered in the optimized device by doping the ETL and HTL. Generally, the conductivity of Spiro-OMeTAD is low, which is improved by doping with additives like 4-tert-Butylpyridine (4-tBP), Bis (trifluoromethane) sulfonimide lithium salt, and FK 209 Co(III) TFSI salt. The V$_{OC}$ of the optimized device was 1.07 V, which corresponds to a more improved processing device from literature [44]. For the optimized device, the doping density of ETL and HTL were selected as 10^{20} cm^{-3}. The efficiency climbed up to 21.62% with optimized doping density of both the transport layers.

Doping the absorber layer with p-type dopants also increases the efficiency [45]. However, doping of the absorber (MAPbI$_3$) is done by changing the ratio of MAI and PbI$_2$ during growing the device which has detrimental effects on the device stability. Unreacted MAI and PbI$_2$ react with moisture and oxygen to deteriorate the device performance. Moreover, the doping density of MAPbI$_3$ perovskite can only be increased up to 10^{14} cm^{-3} [46]. Therefore, the absorber layer was not doped in the optimized device, though it would cause an increase in the device efficiency.

4.6. Effect of temperature and device resistances

Temperature coefficient is another critical parameter for any solar cell. With increased temperature, the efficiency of the cells generally decreases. The temperature coefficient is the change in efficiency per unit temperature change as a percentage of initial efficiency at 25 °C Figure S5 shows the effect of temperature on the efficiency of this model. The temperature coefficient ($\frac{d\eta}{dT}/\eta(25k)$), where η is the efficiency calculated from this curve is 0.186%, which is lower than the value of 0.3–0.5% for silicon solar cells [47]. Lower coefficients suggest that the performance of these cells is good even at higher temperatures, even though they will be degraded if not encapsulated properly.
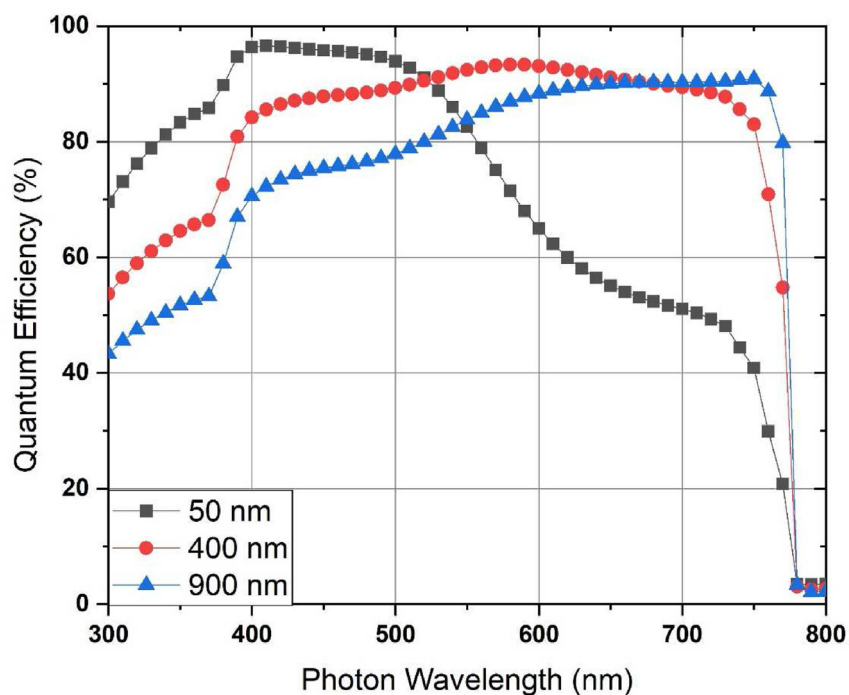
Figure 9. Quantum Efficiency curves of the modelled device for the absorber layer thickness of 50 nm, 400 nm, and 900 nm.
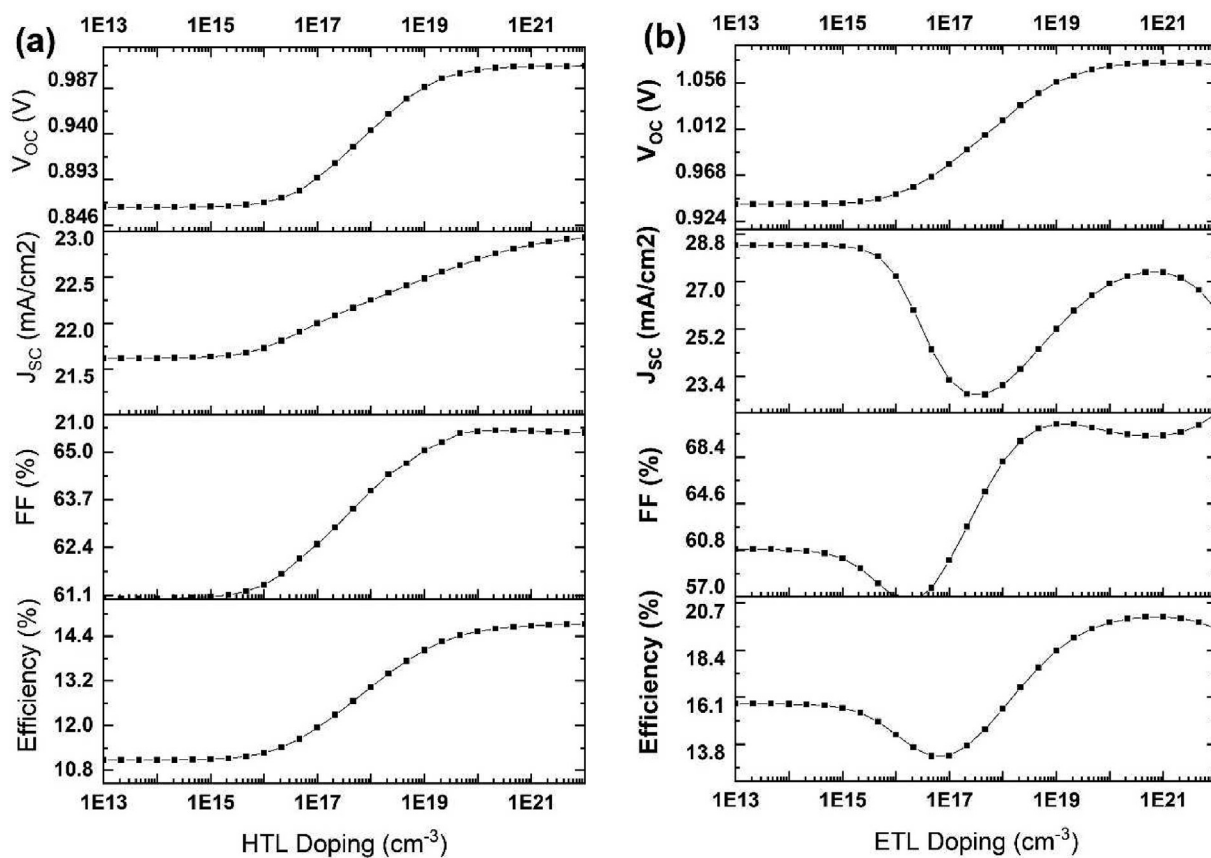

Figure 10. Performance parameters of the modelled device by changing the doping density of (a) HTL and (b) ETL from 10^{13} cm^{-3} to 10^{22} cm^{-3}.

The device can be further optimized by improving the series and shunt resistances. Lower series resistance and higher shunt resistance account for better device performance [48]. The inverse of the slope of the J-V curve near the open circuit area is the numerical measure of the series resistance, and the inverse of the slope near the short circuit area is the measure of shunt resistance. Unlike doping and layer thickness, device resistances cannot be controlled as wished. Improving the values needs better fabrication schemes and material quality. Therefore, the
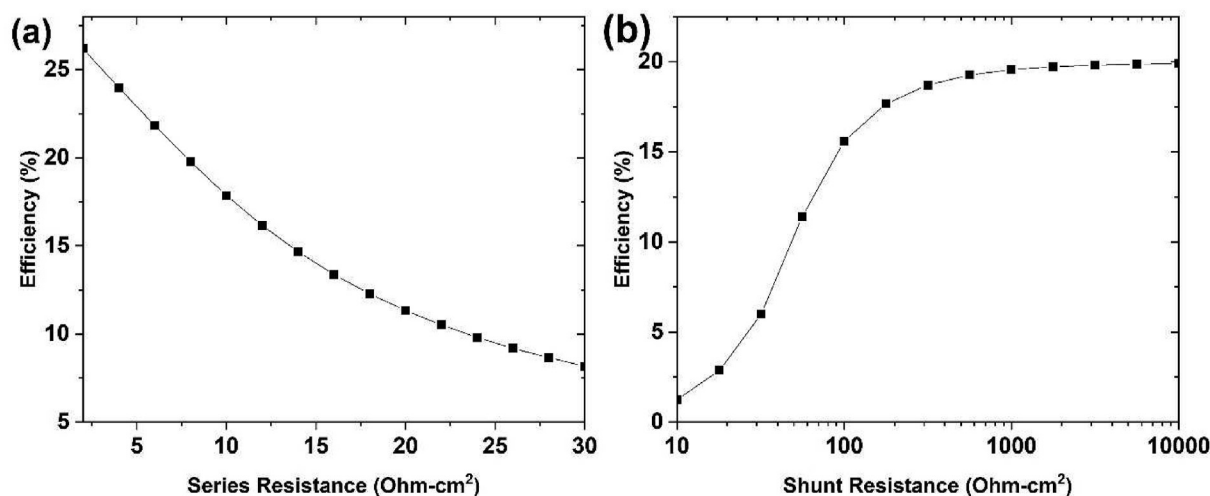
Figure 11. Power Conversion Efficiencies of the optimized device as a function of (a) series and (b) shunt resistances.

device in this work will not be optimized for device resistances. The effect of different series and shunt resistances on device performance is shown in Figure 11(a) and (b). The improvement with optimum series and shunt resistances is primarily due to an increase in fill factor. In the modelled device, the fill factor can be increased up to 80.1% with optimum series and shunt resistances, yielding maximum efficiency of more than 25%. Moreover, the series and shunt resistances are improved with processing techniques and uniformity in the interfaces. If suitable fabrication and device growth can optimize all the parameters, efficiency near the limit for perovskite solar cells can be achieved. Figure 11(a) and (b) shows the performance of the optimized device under different series and shunt resistance. While varying one resistance value, the other was kept fixed to the initial value used throughout this work. Figure 11 shows that shunt resistance greater than 300 Ω-cm^2 is required for achieving high efficiency, while series resistance should be kept as low as possible. Improving the resistances needs suitable contact fabrication and better band alignment.

4.7. Optimized structure and comparison with other material devices

The optimized structure obtained in this study is compared with other devices having different ETL, HTL, or absorber layers. The thickness of the layers, temperature, spectrum, series and shunt resistances are kept constant during this comparison. Figure S6 shows the J-V and Quantum efficiency curves of several devices with a combination of different ETL/Perovskite/HTL layers. For each combination, the performance parameters V_{OC}, J_{SC}, FF and Efficiency are listed in Table 2. The devices with Cu_2O and NiO_x HTLs are simulated with the inverted structure (p-i-n), whereas other devices in Table 2 have conventional n-i-p structure. Cu_2O

and NiO_x are formed via spin coating of their hydroxide or chloride solutions. For dissolving the precursors, ammonium hydroxide and hydrogen peroxide are used as solvents [49]. The J_{SC} and V_{OC} in Table 2 primarily depends on the bandgap of the absorber. With lower bandgap, more photons are absorbed and J_{SC} increases. However, the V_{OC} is decreased for lower bandgap absorbers concurrently. These solvents are not compatible with the perovskites, and thus the films of Cu_2O and NiO_x cannot be spin-coated on top of the perovskite film. Therefore, these two HTLs are used in the inverted structure as simulated in this study in most cases. For different devices, three critical parameters cause the variation in device performance when all other parameters are the same. These are the absorption coefficient of the perovskite layer, the band alignment of ETL and HTL with perovskite, and the charge transport mechanism.

Apart from the absorber layer, the transport layers also play an essential role in the performance of the devices. While J_{SC} is dictated mainly by the absorbance of the perovskite, V_{OC} is affected primarily by the bandgap of the absorber and band offset with the transport layer. The band offsets have a significant role in the FF of the device. In the ETL/Absorber interface, a large valance band offset, and in the Absorber/HTL interface, a large conduction band offset is preferred. This offset will cause only electrons and holes to conduct through the ETL and HTL, respectively and will have a barrier for the opposite type of charge carriers. Figure 12 shows the band structure of different materials used for the simulations. Valence band offset and conduction band offset is visualized in this diagram. For the ETLs, it is expected that they will offer no barrier to the electrons. On the other hand, a significant barrier for holes is required for ETL. In the case of HTL, the opposite properties are expected from ETL. Performance is drastically affected if electrons face a barrier while moving to the ETL and holes while moving to the HTL. The combination Spiro-OMeTAD-FASnI$_3$-ZnO has the lowest efficiency in Table 2 due to the high barrier faced by holes in the FASnI$_3$/Spiro-OMeTAD interface. Such barriers are not present in high-efficiency devices.

5. Conclusion

In recent years, the number of publications involving PSCs has increased rapidly. A good portion of these are simulations with different software. SCAPS is the most used software for PSCs for works involving simulation. However, there is still obscurity regarding different parameters of some materials like FAPbI$_3$, CsFAPb(Br$_x$I$_{1-x}$)$_3$, P3HT and others. Moreover, the simulators still cannot fully emulate the experimental devices due to some non-ideal characteristics of the practical devices. One of these was the reflection, which the simulator assumed as zero. In all the articles published using SCAPS so far, the reflected part was not

Table 2. Performance parameters for different ETL/Absorber/HTL combinations.

Structure	V_{OC} (V)	J_{SC} (mA/cm^2)	FF (%)	Efficiency (%)
ZnO-MAPbI$_3$-Spiro	1.07	26.72	75.54	21.62
ZnO-MAPbBr$_3$-Spiro	1.06	16.27	76.22	13.03
ZnO-CsFAPb(Br$_x$I$_{1-x}$)$_3$-Spiro	0.82	24.45	59.52	11.95
ZnO-FAPbI$_3$-Spiro	1.00	27.27	65.12	17.76
ZnO-FASnI$_3$-Spiro	0.78	26.34	52.46	10.64
ZnO-MAPbI$_3$-Cu$_2$O	1.05	26.55	64.51	17.83
ZnO-MAPbI$_3$-NiO$_x$	1.04	26.54	58.07	16.05
ZnO-MAPbI$_3$-P3HT	0.76	26.41	54.58	10.96
SnO$_2$-MAPbI$_3$-Spiro	1.06	21.94	74.09	17.24
TiO$_2$-MAPbI$_3$-Spiro	1.08	24.49	72.01	18.89
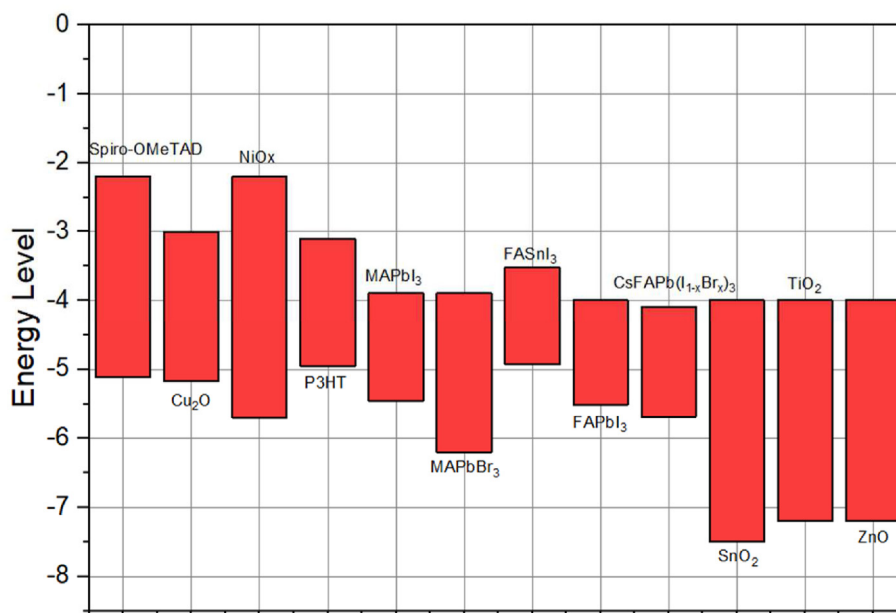
Figure 12. Band diagrams of all the materials used for simulations in this work showing the valence band offset and conduction band offset of different ETL/absorber/HTL combinations.

deducted, which deviated the device performance parameters from experimental values. It was compensated by defects, recombination, and parasitic resistances in most cases. This work improved the simulation credibility by externally calculating the reflectance and feeding the simulator with only the transmitted part. The device is then optimized for the thickness of films, doping, and defects. The effect of the device parasitic resistances and temperature are also shown in the device. Finally, the comparison of the optimized device with different other devices is shown.

One notable future work is to process real devices in the labs based on the optimized devices, including MgF_2 as ARC. It would be interesting to see if the fill factor can also be improved by processing optimizations and additives. The authors predict that future improvement in PSCs will come from improved fabrication methods that will lower the series resistance and higher shunt resistance. For different layer combinations, no (or minimal) barrier for electrons passing to the ETL and holes passing to the HTL will provide better performance. If device resistances, doping and band offset optimization are achieved fully, PSCs may touch the Shockley-Queisser limit for single-junction solar cells.

Declarations

Author contribution statement

Shahriyar Safat Dipta: Conceived and designed the experiments; Performed the experiments; Analyzed and interpreted the data; Contributed reagents, materials, analysis tools or data; Wrote the paper.

Ashraf Uddin, PhD: Conceived and designed the experiments; Analyzed and interpreted the data; Contributed reagents, materials, analysis tools or data; Wrote the paper.

Gavin Conibeer: Conceived and designed the experiments; Analyzed and interpreted the data; Contributed reagents, materials, analysis tools or data.

Data availability statement

Data will be made available on request. The material parameters are listed in Table 1 with references. The absorption coefficients for different materials are taken from PV Lighthouse. Standard AM1.5 spectrum data is taken from National Renewable Energy Laboratory (NREL) website. The simulation data and files that support the findings of this study are available from the corresponding author upon reasonable request.

Declaration of interest's statement

The authors declare no conflict of interest.

Additional information

Supplementary content related to this article has been published online at https://doi.org/10.1016/j.heliyon.2022.e11380.

References

[1] J. Yang, Q. Bao, L. Shen, L. Ding, Potential applications for perovskite solar cells in space, Nano Energy 76 (2020), 105019.

[2] T.-B. Song, Q. Chen, H. Zhou, C. Jiang, H.-H. Wang, Y. Yang, Y. Liu, J. You, Y. Yang, Perovskite solar cells: film formation and properties, J. Mater. Chem. A 3 (2015) 9032–9050.

[3] L. Wang, G.D. Yuan, R.F. Duan, F. Huang, T.B. Wei, Z.Q. Liu, J.X. Wang, J.M. Li, Tunable bandgap in hybrid perovskite CH3NH3Pb(Br3-yXy) single crystals and photodetector applications, AIP Adv. 6 (2016), 045115.

[4] S. De Wolf, J. Holovsky, S.-J. Moon, P. Löper, B. Niesen, M. Ledinsky, F.-J. Haug, J.-H. Yum, C. Ballif, Organometallic halide perovskites: sharp optical absorption edge and its relation to photovoltaic performance, J. Phys. Chem. Lett. 5 (2014) 1035–1039.

[5] L. Lin, L. Jiang, P. Li, B. Fan, Y. Qiu, A modeled perovskite solar cell structure with a Cu2O hole-transporting layer enabling over 20% efficiency by low-cost low-temperature processing, J. Phys. Chem. Solids 124 (2019) 205–211.

[6] S. Iwamoto, Y. Sazanami, M. Inoue, T. Inoue, T. Hoshi, K. Shigaki, M. Kaneko, A. Maenosono, Fabrication of dye-sensitized solar cells with an open-circuit photovoltage of 1 V, ChemSusChem 1 (2008) 401–403.

[7] A. Kojima, K. Teshima, Y. Shirai, T. Miyasaka, Organometal halide perovskites as visible-light sensitizers for photovoltaic cells, J. Am. Chem. Soc. 131 (2009) 6050–6051.

[8] J.Y. Kim, J.-W. Lee, H.S. Jung, H. Shin, N.-G. Park, High-efficiency perovskite solar cells, Chem. Rev. 120 (2020) 7867–7918.

[9] Q. Wali, F.J. Iftikhar, M.E. Khan, A. Ullah, Y. Iqbal, R. Jose, Advances in stability of perovskite solar cells, Org. Electron. 78 (2020), 105590.

[10] A. Ghosh, S.S. Dipta, S.S.S. Nikor, N. Saqib, A. Saha, Performance analysis of an efficient and stable perovskite solar cell and a comparative study of incorporating metal oxide transport layers, J. Opt. Soc. Am. B 37 (2020) 1966–1973.

[11] P. Zhao, M. Yue, C. Lei, Z. Lin, J. Su, D. Chen, C. Zhang, J. Zhang, J. Chang, Y. Hao, Device simulation of organic-inorganic halide perovskite/crystalline silicon four-terminal tandem solar cell with various antireflection materials, IEEE J. Photovoltaics 8 (2018) 1685–1691.

[12] F. Azri, A. Meftah, N. Sengouga, A. Meftah, Electron and hole transport layers optimization by numerical simulation of a perovskite solar cell, Sol. Energy 181 (2019) 372–378.

[13] S. Abdelaziz, A. Zekry, A. Shaker, M. Abouelatta, Investigating the performance of formamidinium tin-based perovskite solar cell by SCAPS device simulation, Opt. Mater. 101 (2020), 109738.

[14] S. Rai, B.K. Pandey, D.K. Dwivedi, Modeling of highly efficient and low cost CH3NH3Pb(I1-xClx)3 based perovskite solar cell by numerical simulation, Opt. Mater. 100 (2020), 109631.

[15] D.-L. Wang, H.-J. Cui, G.-J. Hou, Z.-G. Zhu, Q.-B. Yan, G. Su, Highly efficient light management for perovskite solar cells, Sci. Rep. 6 (2016), 18922.

[16] I. Arabatzis, N. Todorova, I. Fasaki, C. Tsesmeli, A. Peppas, W.X. Li, Z. Zhao, Photocatalytic, self-cleaning, anti-reflective coating for photovoltaic panels: characterization and monitoring in real conditions, Sol. Energy 159 (2018) 251–259.

[17] S.Z. Haider, H. Anwar, M. Wang, A comprehensive device modelling of perovskite solar cell with inorganic copper iodide as hole transport material, Semicond. Sci. Technol. 33 (2018), 035001.

[18] N.M. Khusayfan, M.M. El-Nahass, Study of structure and electro-optical characteristics of indium tin oxide thin films, Adv. Condens. Matter Phys. (2013), 408182.

[19] H. ElAnzeery, O. El Daif, M. Buffière, S. Oueslati, K. Ben Messaoud, D. Agten, G. Brammertz, R. Guindi, B. Kniknie, M. Meuris, J. Poortmans, Refractive index extraction and thickness optimization of Cu2ZnSnSe4 thin film solar cells, Phys. Status Solidi A 212 (2015) 1984–1990.

[20] C.S. Ponseca, T.J. Savenije, M. Abdellah, K. Zheng, A. Yartsev, T. Pascher, T. Harlang, P. Chabera, T. Pullerits, A. Stepanov, J.-P. Wolf, V. Sundström, Organometal halide perovskite solar cell materials rationalized: ultrafast charge generation, high and microsecond-long balanced mobilities, and slow recombination, J. Am. Chem. Soc. 136 (2014) 5189–5192.

[21] S. Manzoor, J. Häusele, K.A. Bush, A.F. Palmstrom, J. Carpenter, Z.J. Yu, S.F. Bent, M.D. McGehee, Z.C. Holman, Optical modeling of wide-bandgap perovskite and perovskite/silicon tandem solar cells using complex refractive indices for arbitrary-bandgap perovskite absorbers, Opt Express 26 (2018) 27441–27460.

[22] S. Karthick, S. Velumani, J. Bouclé, Experimental and SCAPS simulated formamidinium perovskite solar cells: a comparison of device performance, Sol. Energy 205 (2020) 349–357.

[23] Y. Miyazawa, M. Ikegami, H.-W. Chen, T. Ohshima, M. Imaizumi, K. Hirose, T. Miyasaka, Tolerance of perovskite solar cell to high-energy particle irradiations in space environment, iScience 2 (2018) 148–155.

[24] S. Brittman, E.C. Garnett, Measuring n and k at the microscale in single crystals of CH3NH3PbBr3 perovskite, J. Phys. Chem. C 120 (2016) 616–620.

[25] K. Galkowski, A. Mitioglu, A. Miyata, P. Plochocka, O. Portugall, G.E. Eperon, J.T.-W. Wang, T. Stergiopoulos, S.D. Stranks, H.J. Snaith, R.J. Nicholas, Determination of the exciton binding energy and effective masses for methylammonium and formamidinium lead tri-halide perovskite semiconductors, Energy Environ. Sci. 9 (2016) 962–970.

[26] T.M. Koh, T. Krishnamoorthy, N. Yantara, C. Shi, W.L. Leong, P.P. Boix, A.C. Grimsdale, S.G. Mhaisalkar, N. Mathews, Formamidinium tin-based perovskite with low Eg for photovoltaic applications, J. Mater. Chem. A 3 (2015) 14996–15000.

[27] C. Malerba, F. Biccari, C. Leonor Azanza Ricardo, M. D'Incau, P. Scardi, A. Mittiga, Absorption coefficient of bulk and thin film Cu2O, Sol. Energy Mater. Sol. Cell. 95 (2011) 2848–2854.

[28] C.A. Gueymard, D. Myers, K. Emery, Proposed reference irradiance spectra for solar energy systems testing, Sol. Energy 73 (2002) 443–467.

[29] C.A. Gueymard, The sun's total and spectral irradiance for solar energy applications and solar radiation models, Sol. Energy 76 (2004) 423–453.

[30] K. Han, C.-H. Chang, Numerical modeling of sub-wavelength Anti-reflective structures for solar module applications, Nanomaterials 4 (1) (2014) 87–128.

[31] Gang Yeol Yoo, Naufan Nurrosyid, SeungJe Lee, Youngsoon Jeong, Ilsun Yoon, Changwook Kim, Woong Kim, Sung-Yeon Jang, Young Rag Do, Newly developed broadband Antireflective nanostructures by coating a low-index MgF2 film onto a SiO2 moth-eye nanopattern, ACS Appl. Mater. Interfaces 12 (9) (2020) 10626–10636.

[32] M.A. Mahmud, N.K. Elumalai, M.B. Upama, D. Wang, M. Wright, T. Sun, C. Xu, F. Haque, A. Uddin, Simultaneous enhancement in stability and efficiency of low-temperature processed perovskite solar cells, RSC Adv. 6 (2016) 86108–86125.

[33] K. Mahmood, B.S. Swain, A. Amassian, Double-layered ZnO nanostructures for efficient perovskite solar cells, Nanoscale 6 (24) (2014) 14674–14678.

[34] J.-Y. Seo, S. Akin, M. Zalibera, M.A.R. Preciado, H.-S. Kim, S.M. Zakeeruddin, J.V. Milić, M. Grätzel, Dopant engineering for spiro-OMeTAD hole-transporting materials towards efficient perovskite solar cells, Adv. Funct. Mater. 31 (2021), 2102124.

[35] E. Kasparavicius, M. Franckevičius, V. Malinauskiene, K. Genevičius, V. Getautis, T. Malinauskas, Oxidized spiro-OMeTAD: investigation of stability in contact with various perovskite compositions, ACS Appl. Energy Mater. 4 (2021) 13696–13705.

[36] X. Hu, H. Yang, C. Zhang, Y. Ding, W. Li, H. Wang, Z. Zang, Interface modification by ethanolamine interfacial layer for efficient planar structure perovskite solar cells, J. Power Sources 513 (2021), 230549.

[37] F. Izadi, A. Ghobadi, A. Gharaati, M. Minbashi, A. Hajjiah, Effect of interface defects on high efficient perovskite solar cells, Optik 227 (2021), 166061.

[38] N.K. Elumalai, A. Uddin, Hysteresis in organic-inorganic hybrid perovskite solar cells, Sol. Energy Mater. Sol. Cell. 157 (2016) 476–509.

[39] H. Pan, H. Shao, X.L. Zhang, Y. Shen, M. Wang, Interface engineering for high-efficiency perovskite solar cells, J. Appl. Phys. 129 (2021), 130904.

[40] A. Bag, R. Radhakrishnan, R. Nekovei, R. Jeyakumar, Effect of absorber layer, hole transport layer thicknesses, and its doping density on the performance of perovskite solar cells by device simulation, Sol. Energy 196 (2020) 177–182.

[41] N.-G. Park, Perovskite solar cells: an emerging photovoltaic technology, Mater. Today 18 (2015) 65–72.

[42] I. Lee, N. Rolston, P.-L. Brunner, R.H. Dauskardt, Hole-transport layer molecular weight and doping effects on perovskite solar cell efficiency and mechanical behavior, ACS Appl. Mater. Interfaces 11 (2019) 23757–23764.

[43] J.T.-W. Wang, Z. Wang, S. Pathak, W. Zhang, D.W. deQuilettes, F. Wisnivesky-Rocca-Rivarola, J. Huang, P.K. Nayak, J.B. Patel, H.A. Mohd Yusof, Y. Vaynzof, R. Zhu, I. Ramirez, J. Zhang, C. Ducati, C. Grovenor, M.B. Johnston, D.S. Ginger, R.J. Nicholas, H.J. Snaith, Efficient perovskite solar cells by metal ion doping, Energy Environ. Sci. 9 (2016) 2892–2901.

[44] M.K.A. Mohammed, M. Shekargoftar, Surface treatment of ZnO films with carbon nanotubes for efficient and stable perovskite solar cells, Sustain. Energy Fuels 5 (2021) 540–548.

[45] Z. Zhang, C. Wu, D. Wang, G. Liu, Q. Zhang, W. Luo, X. Qi, X. Guo, Y. Zhang, Y. Lao, B. Qu, L. Xiao, Z. Chen, Improvement of Cs2AgBiBr6 double perovskite solar cell by rubidium doping, Org. Electron. 74 (2019) 204–210.

[46] J. Euvrard, Y. Yan, D.B. Mitzi, Electrical doping in halide perovskites, Nat. Rev. Mater. 6 (2021) 531–549.

[47] R. Eberle, S.T. Haag, I. Geisemeyer, M. Padilla, M.C. Schubert, Temperature coefficient imaging for silicon solar cells, IEEE J. Photovoltaics 8 (2018) 930–936.

[48] R. Singh, S. Sandhu, J.-J. Lee, Elucidating the effect of shunt losses on the performance of mesoporous perovskite solar cells, Sol. Energy 193 (2019) 956–961.

[49] S. Chatterjee, A.J. Pal, Introducing Cu2O thin films as a hole-transport layer in efficient planar perovskite solar cell structures, J. Phys. Chem. C 120 (2016) 1428–1437.